

# Numerical modeling of 3D fully nonlinear potential periodic waves

Dmitry Chalikov · Alexander V. Babanin · Elena Sanina

Received: 21 January 2014 / Accepted: 28 July 2014 / Published online: 17 August 2014  
© Springer-Verlag Berlin Heidelberg 2014

**Abstract** A simple and exact numerical scheme for long-term simulations of 3D potential fully nonlinear periodic gravity waves is suggested. The scheme is based on the surface-following nonorthogonal curvilinear coordinate system. Velocity potential is represented as a sum of analytical and nonlinear components. The Poisson equation for the nonlinear component of velocity potential is solved iteratively. Fourier transform method, the second-order accuracy approximation of vertical derivatives on a stretched vertical grid and the fourth-order Runge–Kutta time stepping are used. The scheme is validated by simulation of steep Stokes waves. A one-processor version of the model for PC allows us to simulate evolution of a wave field with thousands degrees of freedom for hundreds of wave periods. The scheme is designed for investigation of nonlinear 2D surface waves, generation of extreme waves, and direct calculations of nonlinear interactions.

**Keywords** Numerical modeling · Stokes waves · 3D nonlinear surface waves · McLean instability · Nonlinear interaction · Hasselmann integral

## 1 Introduction

A numerical investigation of fully nonlinear 1D surface waves is based on conformal mapping. Such approach allows us to reduce the problem to surface equations which can be solved with high accuracy by the Fourier transform method (Chalikov and Sheinin 1998, 2005). Naturally, this method cannot be extended for a case of 3D waves. Majority of the models designed for investigation of the 3D wave dynamics are based on simplified equations. Overall, it is unclear which effects are missing in such simplified models. The most developed methods are based on the full 3D equations and surface integral formulations (Clamond and Grue 2001; Clamond et al. 2005; Fochesato et al. 2006). These methods can be applied both to periodic and nonperiodic flows. The main advantage of such methods is accuracy. The methods do not impose any restrictions on wave steepness, so they can be used for simulations of the waves that even approach breaking (Grilli et al. 2001). However, these methods seem to be quite complicated. Their idea was illustrated by simulations of relatively simple wave fields, and it is unlikely that it can be applied to simulation of a long-term evolution of a large-scale multi-mode wave field. Implementation of a multi-pole technique for a general problem of the sea wave simulations obviously leads to considerable algorithmic difficulties.

Another method for 3D waves includes an elliptic boundary layer problem solved by the finite-difference methods. Such approaches to simulation of the unsteady free surface flows based on the full equations have been under development for at least three decades (see, for example, Asaithambi 1987; Housling and Esseltaine 1975; Yeung 1982). Related applications were later described by Bingham and Zhang (2007). The main advantage of these methods is that it is based on initial equations being transformed into the surface-following coordinate system. The Laplace-type equation obtained by transformation into the sigma-coordinate

---

Responsible Editor: Oyvind Breivik

This article is part of the Topical Collection on the *13th International Workshop on Wave Hindcasting and Forecasting in Banff, Alberta, Canada October 27–November 1, 2013*

---

D. Chalikov (✉) · A. V. Babanin · E. Sanina  
Centre for Ocean Engineering, Science and Technology, Swinburne  
University of Technology, Hawthorn, Victoria 3122, Australia  
e-mail: dmitry-chalikov@yandex.ru

D. Chalikov  
P.P. Shirshov Institute of Oceanology,  
30, 1st Lane, V. I., Saint-Petersburg 199053, Russia

system was solved in Cai et al. (1998) by the iterative conjugate gradient method, using the 3D finite element discretization. The finite-difference multi-grid model for a 3D flow was developed in Engsig-Karup et al. (2009). All of the papers of this group were mostly dedicated to technical applications of the water wave theory, for example, to calculations of a dynamic load on submerged bodies, or to simulation of wave dynamics in a domain with a complicated shape. A long-term evolution of such flows was not simulated; this is why the exact conservation of energy was not the main priority of such models. Applicability of these models to investigations of the nonlinear properties of sea waves is also uncertain.

Currently, the most popular approach is the high order scheme (HOS) model developed by Dommermuth and Yue (1987); West et al. (1987). The HOS is based on a paper of Zakharov (1968), where a convenient form of the dynamic and kinematic surface conditions was suggested. The equations were used by Zakharov, were not intended for modeling but rather for investigation of stability of the finite amplitude waves. In that work, a system of coordinates, where depth is referred to the surface, was used, but the Laplace equation for velocity potential was accepted in its traditional form. The Zakharov (1968) followers, however, accepted this idea literally. They used the two coordinate systems: a curvilinear surface-fitting system for surface conditions and the Cartesian system for calculation of the surface vertical velocity. Analytic solution for the velocity potential in the Cartesian coordinate system is known. It is based on the Fourier coefficients on a fixed level, while the true variables are the Fourier coefficients for the potential on the free surface. Here, problem of transition from one coordinate system to another arises. This problem is solved by expansion of the surface potential into the Taylor series in vicinity of the surface. Accuracy of this method depends on accuracy of estimation of the exponential function  $\exp(k\eta)$  with the finite number of the Taylor series. For small-amplitude waves and for narrow wave spectrum, such accuracy is evidently satisfactory. However, for a case of a broad wave spectrum, which contains many wave modes, the order of the Taylor series should be high. The problem is now that the waves with high wave numbers are superposed over the surface of larger waves. Since the amplitudes of the surface potential attenuate exponentially, the amplitude of a small wave at a positive elevation increases and on the contrary can approach zero at negative elevations.

Let us consider an idealized Phillips spectrum  $a_k = a_1 \omega_k^{-5}$  assigned at frequencies  $\omega_k = k^{1/2}$ ,  $k = 1, 2, 3 \dots$  with the peak wave steepness  $a_1 k_1 = 0.1$  ( $k$  and  $\omega$  are nondimensional wave number and frequency, correspondingly). It is easy to estimate that for the double peak frequency  $\omega/\omega_1 = 2$ , relative accuracy  $10^{-4}$  of projection of the potential to level  $z=0$  can be reached with 6 terms of the Taylor series; for  $\omega/\omega_1 = 3$  with 12 terms; and for  $\omega/\omega_1 = 4$  with 15 terms. A typical order of the Taylor

expansion in the HOS model equals 3–5. It is clear that such setting of the HOS model cannot reproduce high-frequency waves, which fact reduces the nonlinearity of the model. This is why such model can be integrated for long periods, using no high-frequency smoothing. Besides, accuracy of the calculation of the vertical velocity on the surface depends on the full elevation at each point. Hence, the accuracy is not uniform along a wave profile. A substantial increase of the Taylor expansion order can definitely result in numerical instability, due to an occasional amplification of the modes with high wave numbers. A similar point of view was shared by the authors of the method based on the surface integral (Clamond et al. 2005). We should note, however, that comparison of the HOS method based on the West et al. (1987) approach with the method of the surface integral for an idealized wave field (Clamond et al. 2006) shows acceptable results. It was shown in last paper that method suggested by Dommermuth and Yue (1987) demonstrates poor divergence of the expansion for the vertical velocity. Still, applicability of the HOS method for simulation of waves with a broad wave spectrum is unclear.

In this work, we develop a new approach specifically targeted at simulation of long-term multi-mode wave field evolution in the deep ocean. The domain is considered as a small part of an infinitely large basin. In this case, it is possible to use a substantial simplification of the problem, assuming periodicity over horizontal coordinates. In many applications, wave field in such a domain can be presented as a superposition of running harmonic waves with random phases. Such linear approach becomes inapplicable for direct investigation of the wave field evolution, resulting from the nonlinear interactions of waves or from development of a wave field under the action of wind and dissipation.

It is well known that the nonlinear transformation and growth of waves occur over hundreds and thousands of wave periods. It imposes tough restrictions on the model because such modifications of waves should not be obscured with the numerical errors. This means that the model should be exact enough to reproduce such relatively slow spectrum evolution. This condition is well satisfied in the 2D model in the conformal coordinates mentioned above. The 3D waves represent a far more difficult object because it is probably impossible to reduce the problem to the surface problem (in fact, the surface integral method cannot be referred to as a 2D method, since it uses the Green function); hence, the velocity potential should be calculated as a solution of an elliptic equation. The present paper contains description of the numerical model and considers several examples to demonstrate applications of the model. In Section 2, the primary equations, the transformation of coordinates, and some technical problems of the 2D

Fourier approximation are described. Section 3 is dedicated to formulation of the numerical scheme in the nonorthogonal and nonstationary curvilinear coordinates. The results of validation of the approach are also given in Section 4. Results of the long-term simulations of a multi-mode 3D wave field are described in Section 5. The main results and prospects of the investigation are discussed in Section 6.

## 2 Equations and transformation of coordinates

Let us consider a nondimensional form of the principal 3D equations for potential waves written in the Cartesian coordinates, i.e. the Laplace equation for the velocity potential

$$\Phi_{xx} + \gamma^2 \Phi_{yy} + \Phi_{zz} = 0, \quad (1)$$

and two boundary conditions at free surface  $\eta = \eta(x, y, t)$ , i.e. the kinematic condition:

$$\eta_t + \eta_x \varphi_x + \gamma^2 \eta_y \varphi_y - \Phi_z = 0, \quad (2)$$

and the Bernoulli integral:

$$\varphi_t + \frac{1}{2} (\varphi_x^2 + \gamma^2 \varphi_y^2 + \Phi_z^2) + \eta + p = 0, \quad (3)$$

where  $(x, y, z)$  are the Cartesian coordinates system,  $t$  is time;  $\eta(x, y, t)$  describes the single-valued interface, i.e. free surface;  $\Phi$  is the 3D velocity potential and  $\varphi$  is the value of  $\Phi$  at surface  $\eta$ ;  $p$  is the external pressure created by the flow above surface and normalized using the density of water. The subscripts denote partial differentiation with respect to the corresponding coordinate. Taking into account the surface tension effect is quite straightforward. However, in this paper, we are focused on large waves, so the corresponding term in (3) is omitted.

Equations 1–3 are written in nondimensional form by using the following scales: length  $L$  where  $2\pi L$  is the (dimensional) period in the horizontal direction; time  $L^{1/2} g^{-1/2}$  and velocity potential  $L^{3/2} g^{1/2}$  ( $g$  is acceleration of gravity). The pressure is normalized by water density so that the pressure scale is  $Lg$ . Equations 1–3 are self-similar to the transformation with respect to  $L$ . The wave spectrum is normally more or less narrow, that is why it is convenient to introduce different length scales  $L$  and  $L_y$  in the directions  $x$  and  $y$ . Since the equations are solved in square domain ( $0 < \xi < 2\pi$ ,  $0 < \vartheta < 2\pi$ ), ratio  $\gamma = L/L_y$  is included in the equations.

System (1)–(3) is solved as an initial value problem for the unknown functions  $\Phi$  and  $\eta$  with the given initial conditions  $\Phi(x, y, z = \eta(x, y, t = 0), t = 0)$  and  $\eta(x, t = 0)$ . It should be noted that though Eqs. 2 and 3 are written for free surface, there are no straightforward ways to reduce the problem to a 2D problem, since for evaluation of  $\Phi_z$ , the Laplace Eq. 1 should be solved in the domain

$$\{0 < \xi \leq 2\pi, \quad 0 < \vartheta < 2\pi, \quad H < z \leq \eta\} \quad (4)$$

with curvilinear upper boundary which is a function of  $\xi$  and  $\vartheta$ . Integration of the system in the Cartesian coordinates is either quite inaccurate or too expensive computationally and hardly efficient for the time intervals which are much greater than the chosen time scale. This is why the existing numerical models of waves are mostly based on strongly simplified approaches. The periodicity conditions over the “horizontal” coordinates  $\xi$  and  $\vartheta$  are assumed:

$$\begin{aligned} x(\xi, \vartheta, \zeta, \tau) &= x(\xi + 2\pi, \vartheta, \zeta, \tau) + 2\pi, \\ y(\xi, \vartheta, \zeta, \tau) &= y(\xi, \vartheta + 2\pi, \zeta, \tau) + 2\pi, \\ z(\xi, \vartheta, \zeta, \tau) &= z(\xi + 2\pi, \vartheta, \zeta, \tau), \\ z(\xi, \vartheta, \zeta, \tau) &= z(\xi, \vartheta + 2\pi, \zeta, \tau). \end{aligned} \quad (5)$$

Let us introduce the *nonstationary surface-following nonorthogonal* coordinate system:

$$\xi = x, \quad \vartheta = y, \quad \zeta = z - \eta(\xi, \vartheta, \tau), \quad \tau = t \quad (6)$$

where  $\eta(x, y, t) = \eta(\xi, \vartheta, \tau)$  is a moving periodic wave surface given by the Fourier series

$$\eta(\xi, \vartheta, \tau) = \sum_{-M < k < M} \sum_{-M_y < l < M_y} h_{k,l}(\tau) \Theta_{k,l} \quad (7)$$

and  $M$  and  $M_y$  are the numbers of modes in the directions  $\xi$  and  $\vartheta$ , correspondingly, while  $\Theta_{k,l}$  is the function:

$$\Theta_{kl} = \begin{cases} \cos(k\xi + l\vartheta) & -M_x \leq k \leq M_x, \quad -M_y < l < 0 \\ \cos(k\xi) & -M_x \leq k \leq 0, \quad l = 0 \\ \sin(k\xi) & 0 \leq k \leq M_x, \quad l = 0 \\ \sin(k\xi + l\vartheta) & -M_x \leq k \leq M_x, \quad 0 < l \leq M_y \end{cases} \quad (8)$$

If accuracy of the Fourier approximation in both directions is the same, then  $\gamma = M_x/M_y$  is a ratio of the domain sides  $L_x/L_y$  in  $\xi$  and  $\vartheta$  directions. The formulation (8), which contains real coefficients of the Fourier transform in the rectangular matrices, allows us to present amplitudes in a form convenient for compact programming. Form (8) permits simple differentiation over

$\xi$  and  $\vartheta$  of any function  $F$  represented by the Fourier coefficients  $F_{k,l}$  in the Fourier space:

$$\begin{aligned} \frac{\partial}{\partial \xi} \left( \sum_{-M < k < M} \sum_{-M_y < l < M_y} F_{k,l}(\tau) \Theta_{k,l} \right) \\ = - \sum_{-M < k < M} \sum_{-M_y < l < M_y} k F_{-k,-l}(\tau) \Theta_{k,l}, \end{aligned} \quad (9)$$

$$\begin{aligned} \frac{\partial}{\partial \vartheta} \left( \sum_{-M < k < M} \sum_{-M_y < l < M_y} F_{k,l}(\tau) \Theta_{k,l} \right) \\ = - \gamma \sum_{-M < k < M} \sum_{-M_y < l < M_y} l F_{-k,-l}(\tau) \Theta_{k,l}. \end{aligned} \quad (10)$$

Since the ratio of horizontal scales  $\gamma$  is taken into account in the definition of derivative over  $\vartheta$ , it is not included in the equations given below.

The vertical coordinate (6) is constructed for deep water case. As seen, vertical fluctuations of the horizontal coordinates  $\xi$  and  $\vartheta$  do not attenuate with depth. Such fluctuations do not create any approximation problems. However, the lower boundary condition is applied at the variable level  $H = \zeta + \eta$ . Since all variables in wave motion attenuate with depth exponentially, difference between the fixed and fluctuating levels for depth  $|H| \gg |\eta|$  becomes negligible. Possibility of using the coordinates (6) for the finite depth case is mentioned in Conclusion.

### 3 3D deep-water wave model

The main advantage of the surface-following coordinate system is that the variable surface  $\eta$  is mapped onto the fixed plane  $\zeta = 0$ . The 3D equations of potential waves in the system of coordinates (6) at  $\zeta < 0$  take the following form:

$$\eta_\tau = -\eta_\xi \varphi_\xi - \eta_\vartheta \varphi_\vartheta + \left(1 + \eta_\xi^2 + \eta_\vartheta^2\right) \Phi_\zeta, \quad (11)$$

$$\varphi_\tau = -\frac{1}{2} \left( \varphi_\xi^2 + \varphi_\vartheta^2 - \left(1 + \eta_\xi^2 + \eta_\vartheta^2\right) \Phi_\zeta^2 \right) - \eta p, \quad (12)$$

$$\Phi_{\xi\xi} + \Phi_{\vartheta\vartheta} + \Phi_{\zeta\zeta} = \Upsilon(\Phi), \quad (13)$$

where  $\Phi$  is a 3D velocity potential;  $p$  is the external pressure;  $\varphi$  is a value of  $\Phi$  at surface  $\zeta = 0$  while  $\Upsilon(\cdot)$  is the operator:

$$\Upsilon(\cdot) = 2\eta_\xi(\cdot)_{\xi\xi} + 2\eta_\vartheta(\cdot)_{\vartheta\vartheta} + (\eta_{\xi\xi} + \eta_{\vartheta\vartheta})(\cdot)_{\zeta\zeta} - (\eta_\xi^2 + \eta_\vartheta^2)(\cdot)_{\zeta\zeta} \quad (14)$$

Equations 11 and 12 are written at the free surface whose position in the surface-following coordinate system is fixed at  $\zeta = 0$ , as mentioned above. These equations formally look as 2D; however, they include the vertical derivative of the potential  $\Phi_\zeta$  which should be derived from the elliptical Eq. 13 with the following boundary conditions:

$$\Phi(\zeta = 0) = \varphi, \quad \frac{\partial \Phi}{\partial \zeta}(\zeta \rightarrow -\infty) = 0. \quad (15)$$

The second condition (15) in the numerical scheme is replaced by the condition at the finite depth  $\frac{\partial \Phi}{\partial \zeta}(\zeta = H) = 0$  where depth  $H$  should be large enough to be considered as infinitely large. Previous calculations with the 1D model show that such  $H$  can be defined by the formula  $H = 2\pi n/k_p$  where  $k_p$  is wave number of the mode with the largest amplitude, while  $1 < n \leq 2$ .

Equations 11 and 12 were suggested by Zakharov (1968), but the approach has not been extended for the full system of the equations.

The 2D equations for potential waves written in the conformal coordinates have a remarkable property, i.e. the Laplace equation remains the same. This is why the Fourier modes of the velocity potential can be represented through a standard expansion. It means that the potential and any of its derivatives decrease exponentially from the free surface. In a 3D case in the Cartesian coordinates, as well as in the curvilinear coordinates, this is not so. However, it would be reasonable to suggest that the exponential behavior remains dominant, while the potential can be represented as a sum of two components, i.e. the analytic (“linear”) one  $\bar{\Phi}$  ( $\bar{\varphi} = \bar{\Phi}(\xi, \vartheta, 0)$ ) and an arbitrary nonlinear component  $\tilde{\Phi}$ , ( $\tilde{\varphi} = \tilde{\Phi}(\xi, \vartheta, 0)$ )<sup>1</sup>:

$$\varphi = \bar{\varphi} + \tilde{\varphi}, \quad \Phi = \bar{\Phi} + \tilde{\Phi}. \quad (16)$$

The analytic component  $\bar{\Phi}$  satisfies the Laplace equation:

$$\bar{\Phi}_{\xi\xi} + \bar{\Phi}_{\vartheta\vartheta} + \bar{\Phi}_{\zeta\zeta} = 0, \quad (17)$$

with the known solution:

$$\bar{\Phi}(\xi, \vartheta, \zeta) = \sum_{k,l} \bar{\varphi}_{k,l} \exp(|k|\zeta) \Theta_{k,l}, \quad (18)$$

( $\bar{\varphi}_{k,l}$  are the Fourier coefficients of the surface analytical potential  $\bar{\varphi}$  at  $z=0$ ). The solution satisfies the boundary conditions:

$$\begin{aligned} \zeta = 0 : \quad \bar{\Phi} &= \bar{\varphi} \\ \zeta \rightarrow -\infty : \quad \tilde{\Phi}_\zeta &\rightarrow 0 \end{aligned} \quad (19)$$

<sup>1</sup> Note that the term “linear” is conventional, since this component is also influenced by the nonlinearity due to curvature of the surface.

The nonlinear component satisfies the equation:

$$\tilde{\Phi}_{\xi\xi} + \tilde{\Phi}_{\eta\eta} + \tilde{\Phi}_{\zeta\zeta} = \Upsilon(\tilde{\Phi}) + \Upsilon(\bar{\Phi}). \quad (20)$$

Equation 20 is solved with the boundary conditions:

$$\begin{aligned} \zeta = 0 : \tilde{\Phi} &= 0 \\ \zeta \rightarrow -\infty : \tilde{\Phi}_{\zeta} &\rightarrow 0 \end{aligned} \quad (21)$$

Derivatives of the linear component  $\bar{\Phi}$  are calculated directly with the use of (9) and (10). The scheme combines the 2D Fourier transform method in the “horizontal surfaces” and the second-order finite-difference approximation on stretched staggered grid defined by the relation  $\Delta\zeta_{j+1} = \chi\Delta\zeta_j$  ( $\Delta\zeta$  is vertical step, and  $j=1$  at the surface). The stretched grid provides increase of accuracy of approximation for the exponentially decaying modes. Values of the stretching coefficient  $\chi$  lie within the interval 1.10–1.20. Finite-difference second-order approximation of Eq. 20 on a nonuniform vertical grid is quite straightforward. The vertical derivatives of the first and second orders for  $\zeta < 0$  are approximated with the following formulas:

$$\frac{\partial^2 \Phi_{k,l,j}}{\partial \zeta^2} \approx A^1(j)\Phi_{k,l,j-1} + A^2(j)\Phi_{k,l,j} + A^3(j)\Phi_{k,l,j+1} \quad (22)$$

$$\frac{\partial \Phi_{k,l,j}}{\partial \zeta} \approx A^4(j)\Phi_{k,l,j-1} + A^5(j)\Phi_{k,l,j} + A^6(j)\Phi_{k,l,j+1}$$

where

$$\begin{aligned} A^1(j) &= \frac{2\Delta\zeta_{j+1}}{D_j}, \quad A^3(j) = \frac{2\Delta\zeta_j}{D_j}, \quad A^2(j) = -A^1(j) - A^3(j) \\ A^4(j) &= \frac{2\Delta\zeta_{j+1}}{D_j}, \quad A^6(j) = -\frac{2\Delta\zeta_j}{D_j}, \quad A^5(j) = -A^4(j) - A^6(j) \end{aligned} \quad (23)$$

and

$$D_j = \Delta\zeta_{j+1}(\Delta\zeta_j)^2 + \Delta\zeta_j(\Delta\zeta_{j+1})^2. \quad (24)$$

Number of levels  $L_w$  depends on a shape of spectrum, and in the calculations represented below,  $L_w$  varies within the limits  $L_w = 15 \div 100$ . Contrary to the HOS and the surface integral methods, this numerical scheme for 3D wave problem is written directly for the initial system of Eqs. 11–13.

The diagnostic Poisson-like Eq. 20 for the nonlinear component of the velocity potential  $\tilde{\Phi}$  is solved using the tridiagonal matrix algorithm (TDMA, Thomas 1949) generalized for a 3D case through the Fourier presentation over the horizontal coordinates. Term  $\Upsilon(\tilde{\Phi})$  in the right-hand side of Eq. 20 is calculated at each iteration, using the values of  $\tilde{\Phi}$  obtained at the previous iteration. The term  $\Upsilon(\bar{\Phi})$ , as well as

the coefficients that include derivatives of  $\eta$  in the right-hand side of (20), are fixed inside the iterations. The initial  $\tilde{\Phi}$  is equal to zero, while in the process of calculations, this value is taken from the previous time step. The iterations continue until the residual error for Eq. 20 yields accuracy of  $\varepsilon \sim 10^{-9} - 10^{-6}$ , depending on parameters of the vertical grid. Typically, for all calculations considered, the error  $\varepsilon$  decreases exponentially during iterations. Speed of the calculations for a multi-mode wave field is reasonably high if the *rms* steepness does not exceed the value of 0.2. However, the model remains stable even if the local steepness considerably exceeds 1 at certain points.

The suggested scheme has obvious advantages if compared with the schemes that do not use separation into nonlinear and linear parts, i.e. (1) values of  $\tilde{\Phi}$  are two orders less than the values of  $\bar{\Phi}$ ; (2) derivatives  $\bar{\Phi}$  are calculated with analytical accuracy. This is why the number of levels and the prescribed relative accuracy of the solution for  $\tilde{\Phi}$  can be reduced; (3) number of iterations is reduced than compared with the scheme for Eq. 12, so the calculation speed is higher. A typical number of iterations for Eq. 12 for  $\varepsilon = 10^{-7}$  is 5–10, while the number of iterations for Eq. 20 seldom exceeds 2. The 3D solution being found, the Fourier coefficients for the vertical velocity ( $\partial\Phi/\partial\zeta$ )<sub>*k,l,0*</sub> on the surface, are calculated as a sum of the linear and nonlinear components:

$$\left(\frac{\partial\Phi}{\partial\zeta}\right)_{k,l,0} = \sum_{k,l} |k| \bar{\varphi}_{k,l} \Theta_{k,l} + A_1^1 \tilde{\Phi}_{k,l,1} - A_2^2 \tilde{\Phi}_{k,l,2}, \quad (25)$$

where  $A_1^1$  and  $A_2^2$  are the coefficients used for calculation of the vertical velocity at  $\zeta=0$  with the second-order accuracy:

$$A_1 = \frac{\zeta_1}{\zeta_1\zeta_2 - \zeta_2^2}, \quad A_2 = \frac{\zeta_2}{\zeta_1^2 - \zeta_1\zeta_2}, \quad (26)$$

and  $\zeta_1$ ,  $\zeta_2$  are the vertical coordinates of  $\tilde{\Phi}_{k,l,1}$  and  $\tilde{\Phi}_{k,l,2}$ , respectively. Note that  $\tilde{\Phi}_{k,l,0} = 0$  and  $\zeta_0 = 0$ .

The Fourier transform method assumes that all nonlinear terms are calculated on the extended grid  $N \times N_y$  ( $N = 4M$ ,  $N_y = 4M_y$ ) in physical space, the result being transformed into the Fourier space. Description of variables in terms of the Fourier components is more compact than that in terms of the grid values. That is why the Fourier components are considered as the basic presentation, while the grid fields are calculated and stored only when and where they are required.

The asymptotic behavior of  $\tilde{\Phi}_{k,l}$  in the vicinity of  $\zeta=0$  is very close to the linear one, which fact provides high relative accuracy of the order of  $10^{-5} - 10^{-4}$  for the second-order approximation for the vertical derivative in Eq. 20 at  $\zeta < 0$  and for the vertical velocity of the order of  $10^{-7} - 10^{-8}$  on surface  $\zeta=0$ . Profiles of the Fourier amplitudes of linear and nonlinear components are given in Fig. 1. The calculations



were done for initial wave field defined by the Pierson–Moskowitz (1964) spectrum, with  $M_x=256$ ,  $M_y=64$ ,  $L_w=15$  for  $t=500$  (which time corresponds to 100,000 time steps). As seen, the values of  $\tilde{\Phi}_{k,l}$  are by two decimal orders smaller than the values of  $\bar{\Phi}_{k,l}$ .

The model is mostly intended for simulation of the multi-mode long-term wave field evolution with realistic spectrum. No matter how high the spectral resolution might be, for the long-term simulations of nonlinear waves, the energy flux into a truncated part of spectrum ( $\sqrt{k^2 + l^2} > M$ ) must be parameterized. Otherwise, the spurious energy accumulation, violating the energy conservation law at large wave numbers, always corrupts the numerical solution. In numerical solutions of the fluid mechanics equations, this effect is suppressed by introducing different types of viscosity. Thus, the atmospheric models often include purely artificial operators formulated in the Fourier space. A similar scheme was described in the previous articles which considered the conformal method for the direct wave modeling (Chalikov and Sheinin 1998, 2005). Following the scheme, simple dumping terms were added to the right-hand sides of the Fourier form of Eqs. 11 and 12:

$$\frac{\partial \eta_{k,l}}{\partial \tau} = E_{k,l} - \mu_{k,l} \eta_{k,l}, \quad (27)$$

$$\frac{\partial \varphi_{k,l}}{\partial \tau} = F_{k,l} - \mu_{k,l} \phi_{k,l}, \quad (28)$$

where  $E_{k,l}$  and  $F_{k,l}$  are the Fourier coefficients for the right-hand sides of Eqs. 14 and 15, and

$$\mu_{k,l} = \begin{cases} rM \left( \frac{|k| - k_d}{M - k_d} \right)^2 & \text{if } |k| > k_d \\ 0 & \text{otherwise} \end{cases} \quad (29)$$

where  $|k| = \sqrt{k^2 + l^2}$  and  $k_d$  is radius of the domain which is not affected by smoothing. Value of  $k_d$  depends on the spectral resolution and position of the spectrum in the Fourier domain. The value of  $k_d$  is chosen in the interval  $(0.5, 0.9M)$  in different versions of the model. The value of  $r=0.25$  is chosen for all of the runs discussed below, since it was found that the results were reasonably insensitive to the variations of  $r$ . The dissipation effectively absorbs energy at wave numbers close to the truncation number  $M$  and does not affect the energy at wave numbers  $|k| \leq k_d$ . Note that increase of the truncation number  $M$  shifts the dissipation area to higher wave numbers (if  $M \rightarrow \infty$ , the energy sink due to dissipation tends to zero), so the scheme described above retains the approximation of the original (nondissipative) system. Note also that the scheme (27)–(29) is introduced in order to describe a real physical process, i.e. the dissipation of wave energy due to the flux of energy into a truncated part of spectrum. This process is usually very slow. Decay of the total

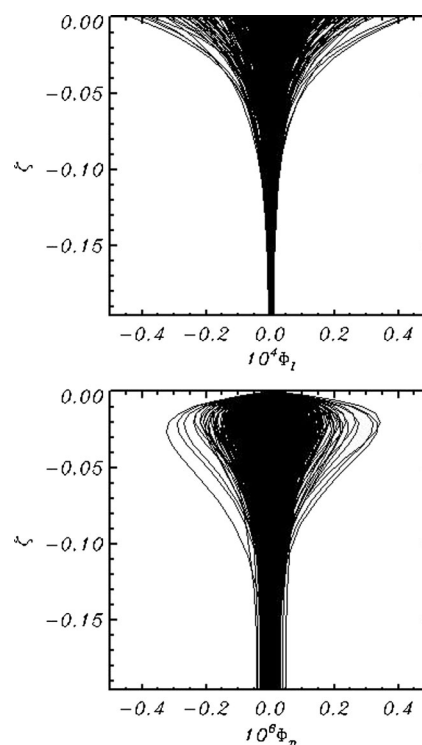


**Fig. 1** Upper panel: vertical profiles of Fourier coefficients for analytic components of velocity potential  $10^4 \bar{\Phi}_l(\zeta)$ ; bottom panel: vertical profiles of Fourier coefficients for nonlinear component  $10^6 \tilde{\Phi}_{k,l}(\zeta)$

energy  $E$  at each time step is of the order of  $(10^{-7} - 10^{-6})E$ , but in the absence of such dissipation, the numerical instability, growing exponentially in the vicinity of  $k=M$ , occurs and finally terminates solution. To avoid such smoothing, for example, a similar model (Zakharov et al. 2002) uses the number of modes  $M=1,000,000$ , which can hardly be considered a rational solution of the problem.

The fourth-order Runge–Kutta scheme was used for time integration of Eqs. 11 and 12. For any explicit time integration scheme, a stability criterion has the form  $\Delta\tau \leq C\omega_{\max}^{-1}$  (if dissipation does not play a significant role), where  $\Delta\tau$  is time step;  $\omega_{\max} = k_{\max}^{1/2}$  is the maximum frequency of the system; and  $C$  is a constant depending on the scheme, for the Runge–Kutta scheme  $C = 2\sqrt{2}$ . We should note that such estimation does not always work in our case because of the strong nonlinear local effects. Finally, the time step was chosen empirically. For example, for  $M=256$  time step used was 0.005.

#### 4 Validation of the 3D deep-water model

No doubt that at a sufficient number of modes in Eqs. 11 and 12 can be integrated in time with the Fourier transform method and Runge–Kutta scheme, with high accuracy. Thus, the critical point of the entire scheme is accuracy of solution of the 3D equations for the velocity potential (20) with the boundary condition (21). There are several methods of

validation of the scheme for Eq. 20. The most straightforward method is based on comparison of the vertical velocity on surface  $\partial\Phi/\partial\zeta$  for 2D problem obtained in the current scheme, with the vertical velocity calculated using the precise scheme based on conformal mapping. Such comparison was done for the Stokes wave with steepness  $ak=0.40$ . Transferring the solution from the conformal coordinates to the uniform-over- $x$  grid was done using the fourth-order periodic spline

$$\Phi(\xi, \vartheta, \zeta) = \sum_{-M_x < k < M_x} \sum_{-M_y < l < M_y} \sum_{1 < i < N_x} \sum_{1 < j < N_y} \varphi_{k,l}^0 \exp(|k|(\zeta + \eta(\xi_i, \vartheta_j))) \Theta_{k,l}, \quad (30)$$

where  $N$  and  $N_y$  are the numbers of grid points in the directions  $\xi$  and  $\vartheta$ , correspondingly;  $\varphi_{k,l}^0$  are Fourier coefficients of the velocity potential at the fixed level  $z=0$ . Equation 30 defines the potential on surface  $\varphi=\Phi(\xi, \vartheta, 0)$  through the Fourier coefficients  $\varphi_{k,l}^0$  in the Cartesian coordinate system for  $z=0$ . Since the coefficients  $\varphi_{k,l}^0$  are unknown, Eq. 30 cannot be used directly for integration of the system (11)–(13). However, Eq. 30 is useful for a detailed validation

interpolation. It was found that the solutions for vertical velocities obtained in 2D and 3D models coincided, the accuracy being of the order of  $10^{-5}ak$ . Note that the two-dimensionality assumption used in such validation does not create a problem, since only the vertical operator is being checked.

The second method of validation is based on solution for Eq. 13:

$$\frac{\partial\Phi}{\partial\zeta}(\xi, \vartheta, 0) = \sum_{-M_x < k < M_x} \sum_{-M_y < l < M_y} \sum_{1 < i < N_x} \sum_{1 < j < N_y} |k| \varphi_{k,l}^0 \exp(|k|\eta(\xi_i, \vartheta_j)) \Theta_{k,l} \quad (31)$$

Such calculations prove that the analytical solution (28) coincides with the results of the numerical solution of Eq. 20, the accuracy being  $10^{-5}-10^{-4}ak$ .

The second method of validation was applied for a wave field defined by JONSWAP spectrum at  $\Omega_p=U_{10}/c_p=2$ , with the directional spreading proportional to  $(\text{sech}(\theta))^4$ , ( $\theta$  is the direction of a mode), which corresponds to steep waves. The exact calculations were made at resolution  $M=128$ ,  $M_y=32$ , number of levels  $L_w=100$ , with accuracy of the solution of Eq. 20 being  $\varepsilon=10^{-10}$ . Then, the solution at a lower resolution was compared with the high-accuracy solution. In Fig. 2, dependence of *rms* error  $E_{rms}$ :

$$E_{rms} = \left( \overline{(w_{100} - w_L)^2} \right)^{1/2}, \quad (32)$$

is given ( $w_{100}$  and  $w_L$  are the grid surface vertical velocities obtained at  $L_w=100$  and at variable  $L_w$ ). As seen, *rms* accuracy  $E_{rms}$  monotonically decreases when approaching the number of levels of  $L_w=100$ .

The methods described above are targeted at validation of the numerical scheme for the elliptic Eq. 20 used at every time step. The most efficient method of validation of both the

of accuracy of its numerical solution. First, arbitrary Fourier coefficients  $\varphi_{k,l}^0$  for the velocity potential at level  $z=0$  are chosen. Then, the velocity potential at free surface  $z=\eta$  is transferred using (30). Values of the velocity potential are used as a surface boundary condition for Eq. 20. The calculated vertical velocity on the surface is then compared with the result calculated directly with Eq. 30

numerical scheme and the codes for Eqs. 11–13 is comparison of the results of integration of Eq. 11–13 with the exact steady solution of the equations obtained in a moving coordinate system. To obtain steady solutions with a very high accuracy (crucial for the model validation), an iterative algorithm was developed on the basis of integration operators and the Hilbert transform in the Fourier space. The scheme uses the Fourier transform method to calculate nonlinearities. Algorithms for calculation of the stationary gravity Stokes waves (Stokes 1847), as well as capillary gravity and capillary waves for deep water, were described in detail in Chalikov and Sheinin (1998). An algorithm of calculation of the Stokes waves for finite depth was developed in Sheinin and Chalikov (2000).

This method is also used in the current paper. The calculations are performed for the Stokes waves propagating along the  $x$ -axis defined at wave numbers  $k=1, 2, 3 \dots M, M_y=0$ . This setting is most appropriate for validation of numerical scheme, since there is no room for development of the Benjamin–Feir instability (Benjamin and Feir 1967). That is, all the modes with wave numbers  $k>1$  represent components (“bound waves”) of the Stokes wave. Similar calculations using the 2D conformal model demonstrate absolute stability of the first 800 modes of the Stokes wave over hundreds of wave periods

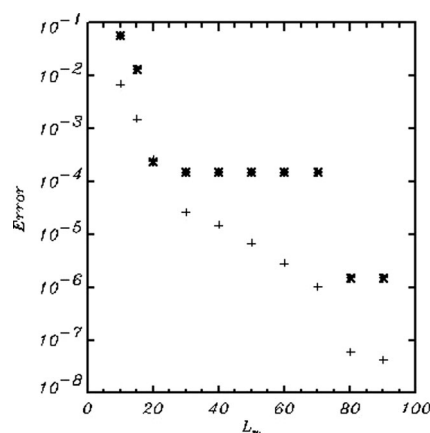


**Fig. 2** Dependence of *rms* error  $E_{rms}$  (32) on the number of levels  $L_w$  (Eq. (20))

(see Chalikov 2005). Note that the Stokes waves can be also assigned at  $k=nk_0$  ( $n$  is a whole number); however, the unavoidable numerical errors finally can play a role of disturbances initiating development of the Benjamin–Feir instability.

Simulation of a very steep Stokes wave with steepness  $ak=0.40$  (assigned in the initial condition) in the current work is performed with parameters  $M=128$ ,  $M_y=16$ ,  $L_w=30$ , and  $\varepsilon=10^{-6}$ . Note that for simulation of the 2D process, number of the lateral modes  $M_y$  can be chosen as 1. Value  $L_y=16$  was used for a purely technical check of the codes, proving that the lateral modes are not generated during integration. The wave surface assigned in the initial condition and that obtained after almost 100 periods of the calculations (10,000 time steps) are shown in Fig. 3. As seen, the surface remains smooth without any signs of disturbances. The theoretical phase velocity of the Stokes wave with steepness  $ak=0.40$  is equal to 1.0822. The phase velocity reproduced with the numerical model is 1.0820. More detailed validations show the time evolution of amplitudes of the first 13 Stokes wave modes (Fig. 4). As seen, the first several modes of the Stokes wave with amplitudes as small as  $10^{-4}$  remain practically unchanged, while the rest of the amplitudes fluctuate. The relative magnitude of fluctuation increases with growth of wave number. However, the average values of amplitudes for each mode do not change, their values decreasing monotonically with growth of wave number. There are no signs of instability which would indicate that the high-order Stokes modes start growing. Evolution of the *rms* difference  $E_{rms}$  between the initial wave surface  $\eta_0$  and the surfaces  $\eta$  simulated in the course of integration

$$E_{rms} = \left( \overline{(\eta_0 - \eta(\tau))^2} \right)^{1/2} \quad (33)$$

is shown in Fig. 5 (top curve). As seen,  $E_{rms}$  is a strictly periodic function of time. When the phases become equalized, the *rms* difference decreases to  $10^{-3}ak$  with no tendency for growing. In reality, the error is smaller, because accuracy of

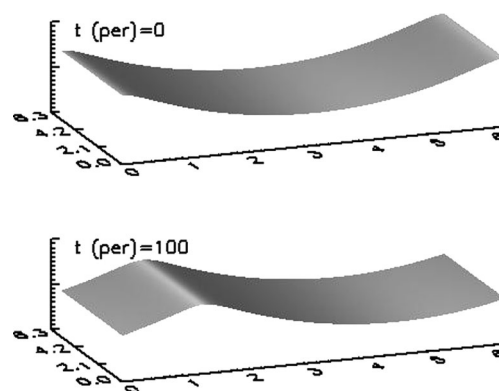


**Fig. 3** Shape of Stokes wave ( $ak=0.40$ ) at  $t=0$  and  $t=100$  periods

coincidence of the surfaces depends on a frequency of sampling. The bottom curve represents a similar *rms* difference between the initial  $\eta_0$  and current waves  $\eta(\tau)$  calculated over the interval between two consequent peaks of the Stokes wave. Since domain  $0 < \xi < 2\pi$  contains only one wave peak, in order to calculate the *rms* difference, the domain was periodically extended over the interval  $-2\pi < \xi < 4\pi$ . As seen, this error fluctuates around the value of  $10^{-3}$  with no tendency for growing.

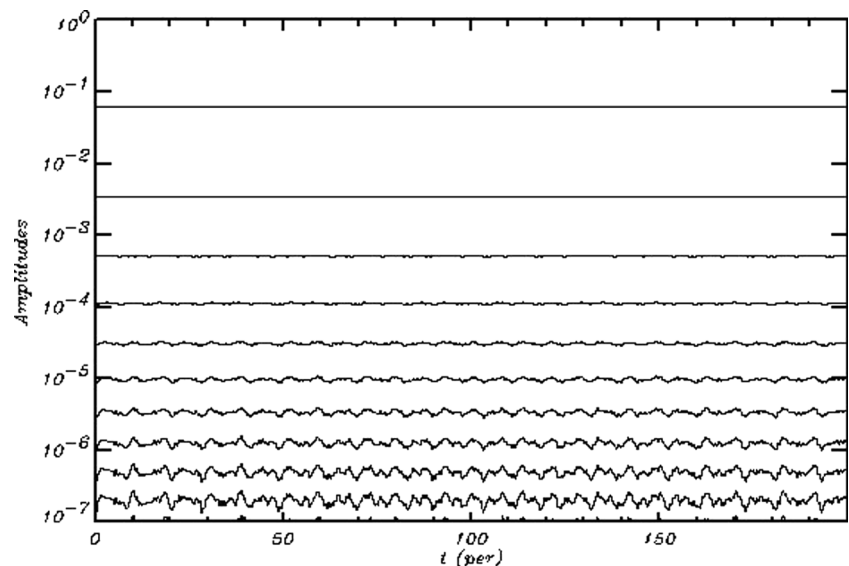
Unlike the 2D model, the 3D model uses a finite-difference approximation for the velocity potential equation. This is why the solution for Stokes wave is not as exact as the same solution in the conformal coordinates. A higher vertical resolution results in a higher accuracy of the solution for the velocity potential, though such calculations certainly become more expensive. Note that this method of validation is full and nontrivial, and the results being combined with the investigation of the numerical scheme for Eq. 20 prove the high accuracy of the entire numerical model. For technical reasons, a similar validation was also done for the Stokes wave propagating along the  $y$ -axis.

In the following numerical experiment, the Stokes wave with steepness  $ak=0.35$  was assigned at wave numbers  $k=8, 16, 24 \dots M$ , while the surface was initially distorted by the random linear waves with amplitudes five decimal orders smaller if compared with the amplitude of the Stokes first mode. The calculations were done in rectangular Fourier domain with dimensions  $M_x=128$  and  $M_y=32$ . Since the modes of the Stokes wave were set over the interval of  $\Delta k=8$ , the noise modes started to grow similarly to the process simulated with the 2D conformal model (Chalikov 2007). The medium steepness  $ak=0.35$  was chosen here, because at large steepness, instability develops too fast.

Evolution of extreme values of steepness is shown in Fig. 6. Absolute values of the negative steepness are larger than those of the positive one, which indicates a forward inclination of the waves linked to the horizontal asymmetry. A wave field finally becomes too steep, while the waves tend to overturn. Unlike the 2D conformal model, which allows us to reproduce the



**Fig. 4** Evolution of amplitudes of steep ( $ak=0.40$ ) Stokes wave  $A_s$  assigned initially at wave numbers  $k=1,2,3,\dots,M$



nonsingle-valued shape of surface, the current model becomes unstable when the local steepness exceeds 1.1. Before this moment, the total wave energy is preserved with very high accuracy. A limiting value of steepness depends on the number of modes and magnitude of a time step.

The initial wave surface and the wave surface prior to breaking are shown in Fig. 7. As seen, the 2D instability leads to formation of a “horseshoe” regular structure well known from the experiments (Su 1982) and numerical simulations based on the surface integral (Fructus et al. 2005).

Evolution of the amplitudes of the first seven modes of the Stokes wave is shown in Fig. 8. Solid lines correspond to the amplitudes of the Stokes modes, while the aggregated gray lines show growing and fast-fluctuating intermediate modes. The main mode with amplitude of  $A_8=0.35$  does not show a

visible change; the amplitudes of all other modes decrease while the intermediate modes are developing by taking energy from all modes of the Stokes wave. The total energy remains constant within the range of six decimal digits.

The 2D wave spectrum prior to breaking (which corresponds to the developed horseshoe quasi-regular structure of Fig. 7), is shown in Fig. 9 (top panel). Since all variables are nondimensional, the spectrum is shown in conventional units, the darkest color corresponding to the maximum of spectral density  $S_m$ , while white color is showing the values less than  $10^{-12}S_m$ . Spectrum in Fig. 9 demonstrates that development of new modes in a 2D case occurs in a more complicated way, i.e. the nearly discrete disturbances develop not at  $l=0$  but rather at some angle to the main modes with wave numbers  $l=\pm 9, 18, 27$ . The main mode of the Stokes wave located at  $k=8$  generates disturbances at the lateral wave number  $l=9$ . Ratio of the wave numbers is  $l/k=1.125$ , which is reasonably close to the value  $l/k=1.15$  found in the linear 2D instability theory of the Stokes wave (McLean 1982). As seen, the full equations also predict development of new rows of modes at  $l=9n$  ( $n=1,2,3,\dots$ ), which corresponds to higher modes of

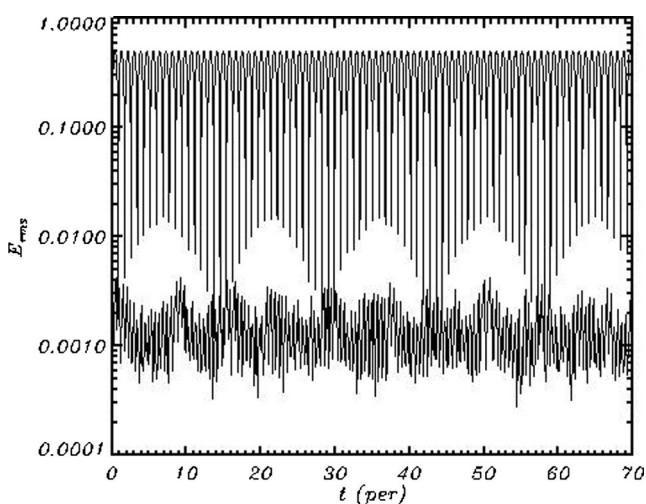


**Fig. 5** Top curve represents evolution of rms difference  $E_{rms}^1$  between the initial wave surface  $\eta_0$  and the surfaces  $\eta$  simulated in the course of integration. Bottom curve corresponds to rms difference between the initial and superimposed wave profiles

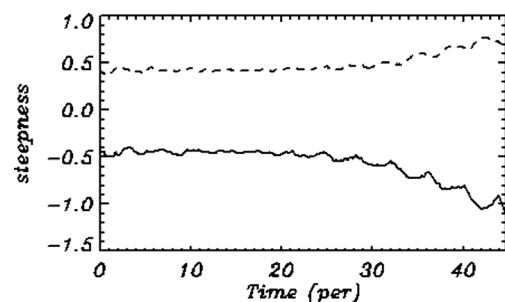


**Fig. 6** Evolution of maximum positive steepness (dashed curve) and minimum negative steepness (solid curve) for a train of Stokes waves,  $ak=0.35$  assigned at wave numbers  $k=8n$ , ( $n=1,2,3,\dots$ ) with imposed disturbances

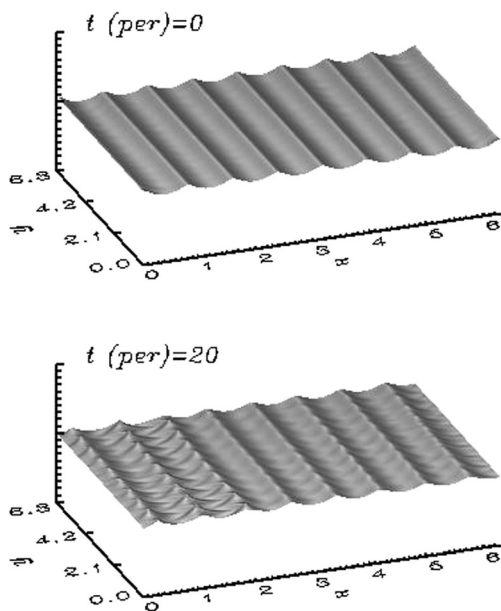


**Fig. 7** Train of Stokes waves ( $ak=0.35$ ) at initial conditions ( $t=0$ ) and a shape of surface just prior to development of numerical instability ( $t=20$  periods)

the Stokes wave. Such evolution of growing modes can be approximated by the expression

$$A_{k,l}(\tau) = A_{k,l}(0) \exp(\beta_{k,l} \omega \tau). \quad (34)$$

Values of  $\beta_{k,l}$  were calculated for  $A_{k,l}(\tau)$  with use of the *rms* method. In the bottom panel of Fig. 9, the local maxima of  $\beta$  are shown by dots whose sizes depend on the magnitude of  $\beta$ . Positions of the original Stokes wave modes are indicated by crosses. Figure 9 shows that the disturbances are located symmetrically with respect to  $k$  axis.

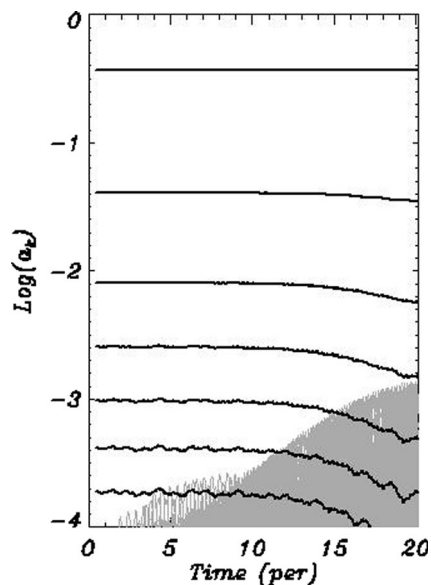


**Fig. 8** Evolution of amplitudes of Stokes wave ( $ak=0.35$ , solid curves) assigned initially with superimposed noise. Aggregated gray lines correspond to new growing modes

## 5 Simulation of a multi-mode wave field

The third series of the calculations was performed to simulate a multi-mode wave field initially defined as a superposition of linear modes with random phases, corresponding to the Pierson–Moskowitz (1964) spectrum with directional spreading in the energy-containing part of the spectrum proportional to  $(\text{sech}(\theta))^4$ . The simulations were performed in rectangular domain with number of modes different in  $x$  and  $y$  directions, i.e.  $M_x=256$ ,  $M_y=64$ . In this case, the grid includes 564,288 knots (130,302 degrees of freedom). All the calculations were conducted on a Dell workstation.

Peak of the spectrum was initially placed at  $(k,l)=(64,0)$ . The calculations with time step  $\Delta\tau=0.0025$  were performed up to the nondimensional time  $\tau=250$  (10,000 time steps), which time corresponds to 318 peak wave periods.

Over such a long period of integration, the energy of waves in the absence of any energy input decreases due to the flux of energy into the subgrid domain as described above. The Pierson–Moskowitz spectrum corresponds to statistically steady wave regime, when the total energy input equals the total energy dissipation. This balance can be introduced by using the energy input from wind, as formulated in Chalikov and Rainchik (2011), as well as the energy dissipation through

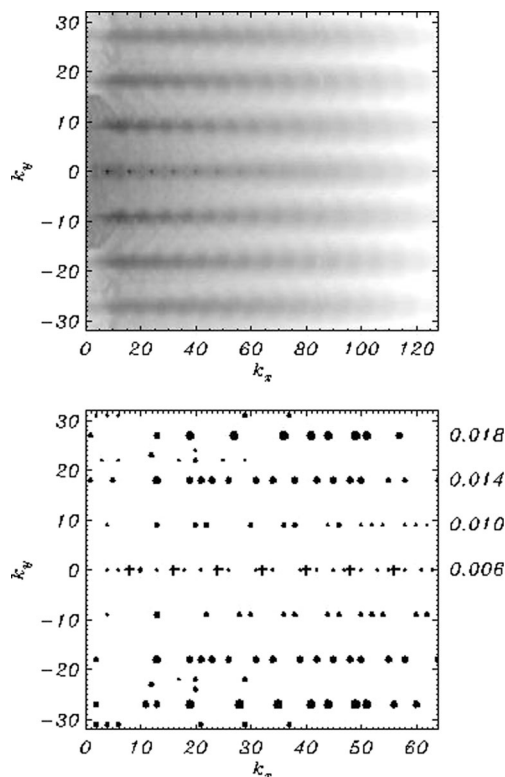


**Fig. 9** Top panel: 2D wave spectrum (conventional units) prior to development of breaking (see Fig. 7). Bottom panel: rate of development  $\beta$  of intermediate mode amplitudes (Eq. 25). The values of  $\beta$  are given outside the frame for each row. Crosses indicate the initial position of Stokes wave modes

the breaking adjustment as suggested in Chalikov and Sheinin (2005). In any case, at present stage, implementation of a complicated physics seems premature. This is why a quasi-stationary regime is reproduced on the basis of a simple scheme designed to preserve the total energy. It is done by introduction of additional terms in the spectral form of Eqs. 11 and 12:

$$\frac{\partial \eta_{k,l}}{\partial \tau} = H_{k,l} + (1-\gamma)\eta_{k,l}, \quad (35)$$

$$\frac{\partial \varphi_{k,l}}{\partial \tau} = F_{k,l} + (1-\gamma)\varphi_{k,l}, \quad (36)$$

where  $\eta_{k,l}$  and  $\varphi_{k,l}$  are the Fourier amplitudes for  $\eta$ , while  $H_{k,l}$  and  $F_{k,l}$  are the Fourier amplitudes of the right-hand sides of Eqs. 11 and 12, including additional terms introduced by (27)–(29);  $\gamma$  is coefficient:

$$\gamma = (E/E_0)^{1/2}, \quad (37)$$

and  $E_0$  is the initial total wave energy equal to the sum of kinetic and potential energies;  $E$  is the total energy at the previous time step. Since the coefficient  $(1-\gamma)$  is very small (of the order of  $10^{-6}$ ), the algorithm (35)–(37) supports the total energy with accuracy of the order of  $10^{-6}$ , which practically does not change a structure of the solution either in the Fourier space or in the physical space. Note that the algorithm (35)–(37) is designed to compensate attenuation of energy due to the flux to the high wave number range.

For a typical peak wavelength, corresponding to the Pierson–Moscowitz spectrum, the horizontal size of domain is of the order of several kilometers. The domain includes too many waves, which is why Fig. 10 shows a 1/64 part of the computed wave surface for  $\tau=250$ . Visually, the surface reminds a natural ocean wave surface. Animations generated in the course of integration depict a highly authentic wave field. After just one peak wave period, the initially sinusoidal waves obtain a typical Stokes-like shape with sharp crests and flat troughs. The probability of surface elevation (normalized by significant wave height) is shown in Fig. 11. For the calculations, 655,360,000 values of  $\eta_{i,j}$  were used. The dashed line represents a reflected branch of the probability distribution for negative  $z$ . As seen, the probability of positive elevation (wave crests) is considerably larger than that of the negative one (troughs), exactly as in the 2D modeling. The thin line in Fig. 11 corresponds to the Gaussian distribution. As seen, the negative values of  $\eta$  have a smaller probability than the Gaussian distribution predicts, while the probability of the positive values  $\eta$  considerably exceeds the Gaussian probability. It can be explained by the tendency of waves to approach the Stokes-like shape. This feature also explains the mechanism of wave breaking and extreme wave generation. Some of the waves change their

shape so significantly that they become unstable. It happens without a noticeable exchange between the modes, with no sign of modulational instability found (see Chalikov 2009). The integral probability of wave trough-to-crest height  $\tilde{H}_f = H_f/H_s$  ( $H_s$  is significant wave height) is shown in Fig. 12. As seen, a wave with a nondimensional height  $\tilde{H}_f > 2.1$  can emerge as frequently as one among one thousand waves. Naturally, to be really “freak”, a wave should be large in the physical space. The largest value of  $\tilde{H}_f$  was equal to 2.71.

Evolution of kinetic (solid curve) and potential (dashed curve) energies are shown in the top panels of Fig. 13 as percentage of the total energy divided by two. To make the figure clearer, only ten successive peak wave periods of the initial and final intervals are shown. The potential and kinetic energies fluctuate considerably (up to 1 %) over the period of adjustment of the linear initial conditions to the nonlinearity. These fluctuations fall in the range of the order of 0.1 %, almost over the entire period of integration. Sum of potential and kinetic energies is preserved with accuracy of the order of  $10^{-5}$ . In the bottom panel of Fig. 13, evolution of skewness (solid line) and kurtosis (dashed line) are given. During the initial period, fast transformation of the elevation and the surface potential (initially assigned according to the linear theory) occurs. Then, the system enters a quasi-stationary regime maintained for most of the integration time. Both skewness and kurtosis (exceeding 3) are positive, which is a particular feature of the nonlinear waves.

It is generally accepted that the linear dispersion relation  $k=\omega^2$  ( $k$  and  $\omega$  are the nondimensional wave number and frequency) is valid in a broad range of wave frequencies. The experimental data, however, confirm applicability of this formula to the relatively low frequencies. The numerical model gives us an opportunity to investigate this problem in more detail.

For the short time periods, when the rate of amplitude  $|h_{k,l}|$  change is small, i.e.

$$\frac{\partial |h_{k,l}|}{\partial \tau} \ll \omega_{k,l} |h_{k,l}| \quad (38)$$

the mode evolution is described by the following relation:

$$\eta(\xi, \vartheta, \tau) = \sum_{k,l} h_{k,l} \theta_{k,l}(k\xi + l\vartheta - \omega\tau), \quad (39)$$

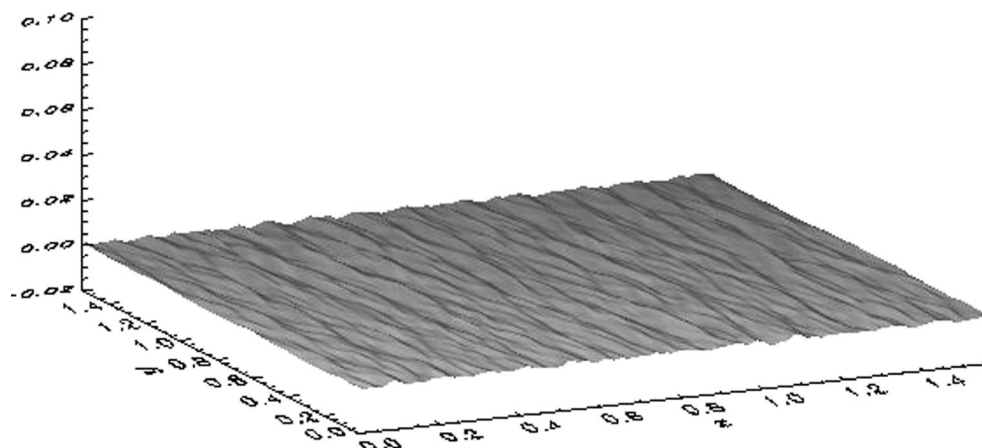
which gives

$$\frac{\partial \eta}{\partial \tau} = \sum_{k,l} \omega_{k,l} h_{-k,-l} \theta_{k,l}(k\xi + l\vartheta - \omega_{k,l}\tau); \quad (40)$$

and the instantaneous value of frequency can be calculated as follows:

$$\omega_{k,l} = \frac{h_{k,l}^*}{h_{-k,-l}}, \quad (41)$$

**Fig. 10** Example of the surface obtained at 318 periods of simulation of a wave field assigned initially with Pierson–Moskowitz spectrum. 1/64 part of the entire surface is shown



where the notation  $h_{k,l}^\tau = \frac{\partial h_{k,l}}{\partial \tau}$  is used. Calculations with the use of (41) give large scatter. This is why the *rms* method for calculating averaged values of frequency  $\bar{\omega}_{k,l}$  is used

$$\bar{\omega}_{k,l} = \frac{\overline{h_{k,l}^\tau h_{k,l}}}{\overline{h_{k,l}^2}}. \quad (42)$$

Accuracy of this method was verified with the  $h_{k,l}$  and  $h_{k,l}^\tau$  data, generated by the linear version of the model which was integrated over several tens of the peak wave periods. It was found that for this case, formula (42) satisfies the linear dispersion relation  $k=\omega^2$  with very high accuracy. Note that the waves with the same wave numbers running in opposite directions cannot be separated, i.e. formula (42) gives absolute values of frequency. In this particular case, it is not important, since the energy of opposite waves is very small. It was found that deviation from the linear dispersion relation depends on the energy of mode, i.e. the less the energy, the stronger the deviation. These effects are demonstrated in Fig. 14 where the spectral density of energy is plotted in the coordinates

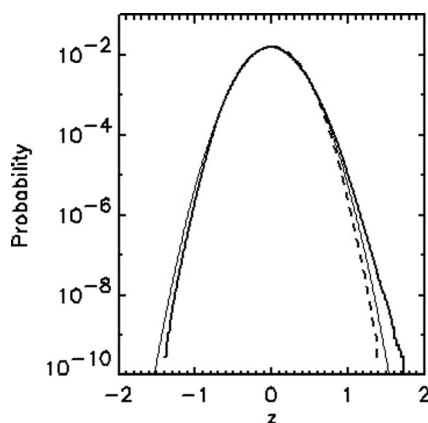


**Fig. 11** Probability of surface elevation. Thick curve corresponds to the model result, while dashed curve corresponds to the reversed probability distribution for negative values  $z$ ; thin curve represents Gauss distribution

$(\omega_{lin}, \omega_{mod})$  where  $\omega_{lin}=k^{1/2}$  and  $\omega_{mod} = \bar{\omega}$ . Different levels of energy (normalized by its maximum) are shown by different densities of the gray tone. The solid curve shows the spectral energy distribution averaged over equal values of  $\omega_{lin}$ , i.e. over directions. As seen, the modes with the large energy obey the linear dispersion relation, i.e. the large energy is concentrated along the straight line  $\omega_{lin}=\omega_{mod}$ , while starting approximately from  $0.1S_p$  ( $S_p$  is a peak value of spectrum), the calculated frequency  $\omega_{mod}$  is mostly larger than the linear frequency  $\omega_{lin}$ . This effect was discovered experimentally, being reproduced in numerical models and explained in Lake and Yuen (1978); Chalikov and Sheinin (1998). In reality, surface waves are nonlinear, each wave being constructed from a carrying mode and the so-called bound waves. These waves are not real waves; they are just shorter modes moving with the speed of the main mode. Besides, a wave field contains free small amplitude waves whose phase velocity is close to the linear phase velocity  $c=\omega/k$ . Consequently, at each wave number, the free waves and bound waves coexist. Their averaged calculated frequency is larger than the

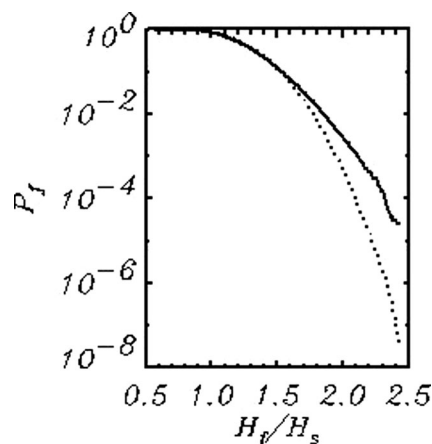
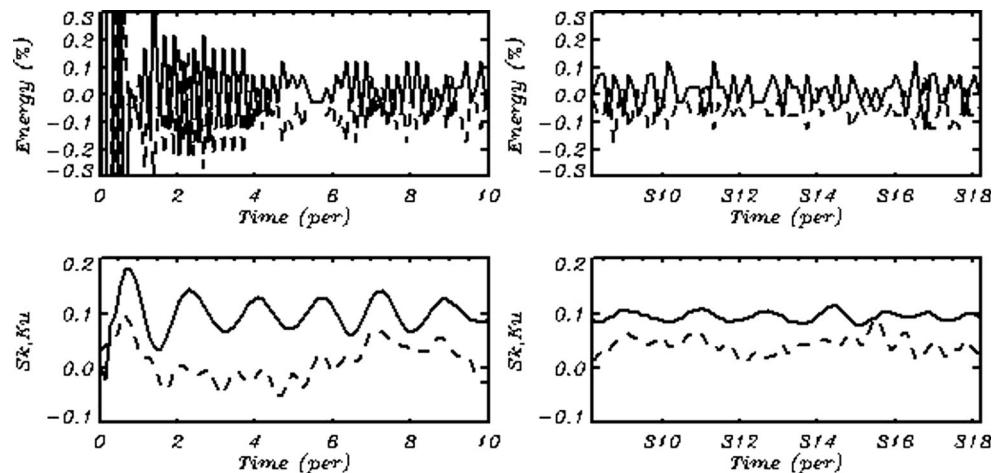


**Fig. 12** Thick curve shows the integral probability of trough-to-crest wave height  $H_T$  normalized by significant wave height  $H_s$ . Thin curve corresponds to Rayleigh distribution



**Fig. 13** The *top panels* represent evolution of kinetic (*solid curve*) and potential (*dashed curve*) energies; the *bottom frames* show skewness (*solid curve*) and kurtosis (*dashed curve*) of wave surface. The *left panels* correspond to the first ten peak wave periods, the *right panels* represent the last ten peak wave periods



linear frequency  $\omega_{lin}$ . This effect is pronounced more clearly if the total nonlinearity is large, while the energy of free waves remains small.

The most curious property of the surface waves is demonstrated in Fig. 15. The spectrum assigned in the initial conditions is smooth (top panel). However, after just several peak wave periods, the spectrum starts transforming, i.e. sharp peaks and deep holes appear. Finally, a continuous spectrum transforms into a nearly discrete one which consists of individual peaks. It is tempting to explain this phenomenon on the basis of the wave–wave resonance mechanism, i.e. the resolution is not high enough to cover all possible resonant combinations of wave numbers and frequencies. This explanation, however, should be based on the assumption that exact dispersion relation is valid. In reality, the phase velocity of each wave mode is fluctuating due to many reasons, such as nonlinearity, Doppler effects, presence of bound waves, etc. Consequently, the resonant conditions can get blurred over a finite area, and therefore, such an explanation is not valid. If it was, the spectrum should be continuous. Moreover, if the resolution was a problem, then, following its increase, the spectrum would have been converging to the continuous spectrum similar to that in the top panel of Fig. 15, which actually does not happen. Note that similar results were obtained using a simplified model based on the equations derived through expansion of the Hamiltonian up to the fourth order (Zakharov et al. 2002). The simplified approach allowed the authors to use a resolution several times higher than that used in the current work. However, simulation of an evolution of the initially homogeneous spectrum resulted in a strictly discrete spectrum similar to that in Fig. 15. It should be noted that the discretization effect can be visible in the 2D Fourier wave number space, while this effect manifests itself much weaker in a single-point low-resolution frequency spectrum.

Another hypothesis of the wave spectrum tendency for discretization is based on consideration of a convergence problem. Actually, the nonlinear interactions occur in the orbital

velocity field. A change of the spectral resolution results in modification of the statistical characteristics of the elevation and velocity fields. It is quite obvious that with increase of the spectral resolution (provided that the total energy conservation is strictly valid), the statistical properties of the velocity and elevation fields cannot formally come to any reasonable limit. It means that the physical mechanism that prevents homogenization of spectrum does exist. Probably, the modes with very close wave numbers cannot exist independently; hence, a wave spectrum consists of a finite number of the nonlinear modes rather than from an infinite number of the linear modes (see also Babanin et al. 2014). In other words, a wave field probably has a “corpuscular nature”. This can be a real cause of the “Manhattan-like” shape of the 2D spectrum in Fig. 15.

It is interesting to note that locations of peaks in spectrum are not fixed; the peaks can slowly migrate in the Fourier space. This effect is illustrated in Fig. 16 where a temporal evolution of amplitudes of 25 modes in the vicinity of the initial peak  $(k_x, k_y) = (64, 0)$  is represented. The curve seems thick because of the high-frequency fluctuations of unknown nature. Probably, these fluctuations are caused by a fast exchange between the potential and kinetic energies visible in Fig. 13 (top panel). Such fluctuations were also observed in the calculations with an exact 1D conformal model. As seen, each mode in the process of evolution changes its location quasi-periodically up to several times. The total change of amplitudes over the entire period reflects downshifting.

Looking at the details of consequent spectra, it is possible to see that each peak undergoes the quasi-periodic fluctuations. The data on the spectrum evolution are used for calculations of the nonlinear spectrum transformation rate  $N$

$$\frac{\Delta S_{k,l}}{\Delta t} = N_{k,l}, \quad (43)$$

where  $\Delta S_{k,l}$  is a change of spectral density over time  $\Delta t$  and  $N_{k,l}$  is an average rate of evolution of the spectral density



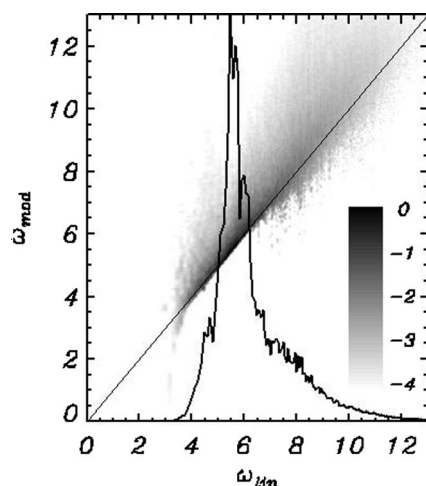


**Fig. 14** Distribution of spectral energy  $\log_{10} \bar{S}$  ( $\bar{S}$  is spectral density, normalized by its maximum) in the coordinates  $(\omega_{lin}, \omega_{mod})$ , where  $\omega_{lin} = k^{1/2}$  and  $\omega_{mod} = \bar{\omega}$  (Eq. 40). Solid line shows the spectral density averaged over directions

due to the nonlinear interactions. In Fig. 17, spectrum  $\bar{N}_k^l$  integrated over the lateral wave numbers  $k_y$ , is shown (slightly smoothed over the wave numbers). As seen, the shape of  $\bar{N}_k^l$  is qualitatively similar to the results of the calculations based on the Hasselmann's integral. The energy in the front slope of the spectrum increases, while the energy in the back slope of the spectrum decreases providing downshifting. Unfortunately, all the available schemes for the Hasselmann's integral

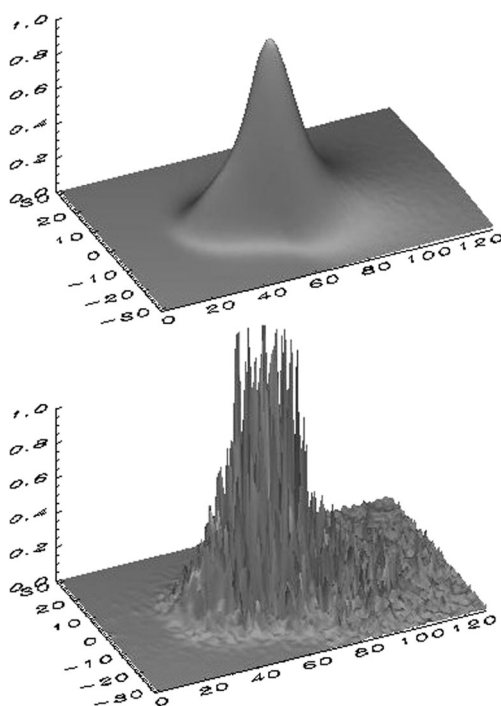


**Fig. 15** Top panel corresponds to the initial Pierson–Moskowitz 2D wave spectrum  $\log_{10}(S)$ . Bottom panel corresponds to the final spectrum after integration over 318 peak wave periods

calculations do not allow us to perform any calculations for such a high resolution used in the present work.

The nonuniformity of a wave spectrum is convenient to estimate with parameter  $J$

$$J = \frac{\sum_{k,l} S_{k,l}^{-1} (\overline{\Delta S_{k,l}^2})^{1/2}}{\overline{S_{k,l}}} \quad (44)$$

which characterises a ratio of the local dispersion of spectrum  $(\overline{\Delta S_{k,l}^2})^{1/2}$  (calculated over four adjacent points) and the central value of spectrum  $S_{k,l}$  averaged over the entire spectrum. When the spectrum is smooth, the value of  $J$  is small and  $J$  approaches 1 when the local differences are of the order of the local values of spectrum. An evolution of  $J$  calculated for 50 runs is shown in Fig. 18. The initial spectra for all the runs were identical, but the wave fields were assigned with different random sets of phases. As seen, the rates of  $J$  growth in different runs were close to each other, while  $J$  increases from  $J=0.1$  up to  $J=0.48$ – $0.55$  and preserves a tendency for further growth. Such high values of  $J$  indicate that the patchiness of spectrum is a typical phenomenon of a simulated wave field. The data obtained in different runs allow us to compare the spectra calculated with the model to the end of each run at 94th peak wave period. The results of such comparison are given in Fig. 19. The gray curves correspond to different runs; the solid curve corresponds to the averaged over ensemble spectrum, while the dashed curves correspond to dispersion. As seen, the difference between the spectra is very large, which means that the evolution of spectrum depends on a set of the initial phases. The locations of peaks and holes are different in different runs. It is confirmed by Fig. 20 where in the top panel, the positions of the local maxima in a wave spectrum are shown. To the local maxima, we refer all points where the value of spectrum exceeds the values in all eight surrounding points. To make the plot clearer, only the points where the spectral density in the central point exceeds  $0.01 S_p$  ( $S_p$  is the peak spectral density) are included. The data in the top panel refer to a

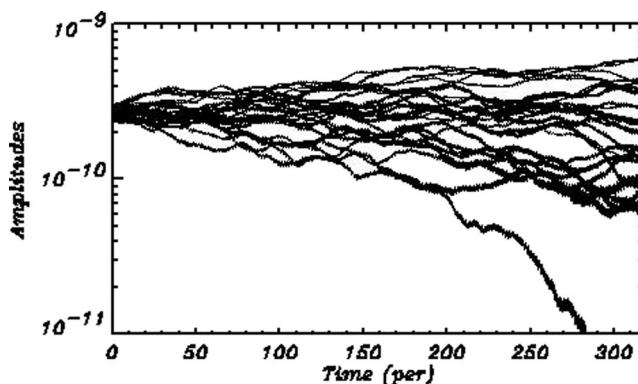


**Fig. 16** Time evolution of 25 Fourier amplitudes in the vicinity of the initial wave peak

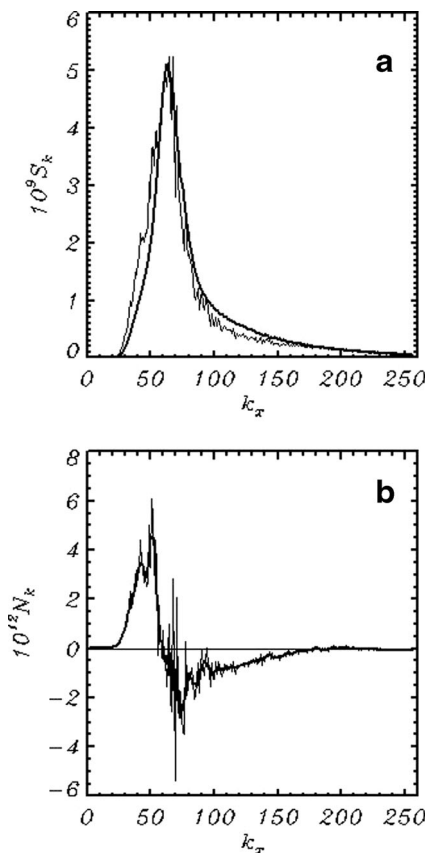


**Fig. 17** **a** Wave spectrum integrated over lateral wave numbers  $k_y$ . *Thick line* shows the initial wave spectrum, and *thin line* shows the final wave spectrum obtained by 318th wave period. **b** *Thin curve* represents spectrum of a nonlinear interaction rate integrated over lateral wave numbers  $k_y$  (see Eq. (27)), *thick curve* shows the same but smoothed spectrum

single spectrum, and the data in the bottom panel include the points for all of the 50 spectra. As seen, the points in the bottom panel are distributed over the wave number space more or less evenly. Note that the maxima change their location also during a single long integration, but this process is

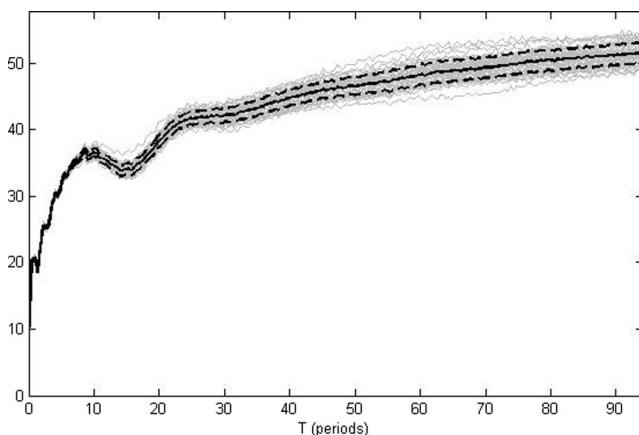


**Fig. 18** Temporal evolution of “patchiness” index (Eq. 37). *Thin curves* correspond to the data obtained in parallel runs, *thick curve* shows the averaged over ensemble data, *dashed curves* characterize dispersion of the data

very slow, i.e. the uniformity shown in the bottom panel of Fig. 20 can be reached over thousands of peak wave periods. These results completely turn down the idea that the peaks and holes can be explained by the resonance mechanisms.

Upon completing this paper, we received Reviewer’s recommendation to reproduce the results obtained with the 3D MNLS model (Dysthe et al. 2003) where evolution of a narrow bandwidth spectrum assigned by the Gaussian distribution in the 2D Fourier space was calculated using the nonlinear 2D Dysthe equation (Dysthe 1979). The initial conditions for spectrum were assigned according to Eq. 7 in the work cited, i.e. the width of spectrum was 0.2 and steepness was 0.1. The number of modes, along  $x$ - and  $y$ -axis’s, was equal to 128; the total number of the Fourier modes was 66,049; the number of grid points was 262,144. The first runs were done when a maximum of spectrum was initially located at  $k_p=64$ ,  $l_p=0$ , but in this case, the spectrum showed an unrealistic behavior at high wave numbers, since the energy was suppressed by dumping (27)–(29) introduced to support stability. In the next runs, a maximum of the spectrum was shifted to position  $k_p=32$ ,  $l_p=0$ . As well as in the work cited above, the results are obtained by averaging over ensemble of 20 runs for various sets of the initial random phase distribution. The spectrum simulated with our model is compared with the spectrum obtained with the Dysthe’s model in Fig. 21. As seen, both of the models identically reproduce the angle widening of spectrum. An asymmetry of this evolution can be explained by different wave steepness in the high-frequency and low-frequency parts of spectrum, i.e. the root-mean-square steepness of the initial wave field is equal to 0.073, while the steepness formed by the modes with wave numbers  $k \leq k_p$  is equal to 0.042 and by the modes with wave numbers  $k \geq k_p$  is equal to 0.063. Crowding of contours at panel *a* in Fig. 20 can be probably explained by using a filter outside the domain:

$$\left(\frac{k-k_p}{k_p}\right)^2 + \left(\frac{l}{k_p}\right)^2 = 1, \quad k > k_p$$

A qualitatively similar effect was observed in our calculations with  $k_p=64$ . We found that the location of spectrum at  $k_p=32$  provided room for smooth developing of spectrum toward high wave numbers. Hence, the computational domain in panel *b* has the size  $4 \times 4$ , while in panel *a* it is  $2 \times 2$ . The spectrum obtained in Dysthe et al. shows downshifting. The same effect was obtained in our calculations. The low-energy “horns” in a low wave number part of spectrum *b* (Fig. 20) was never reproduced in our calculations, probably because of an insufficient resolution at low wave numbers. As a whole, it can be concluded that our results are in a reasonable qualitative agreement with the results of Dysthe et al. (2003). More detailed comparison of our model with the Dysthe (1979)

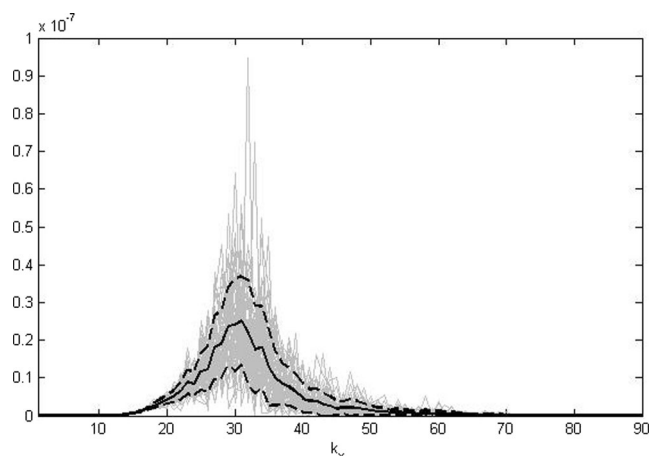


**Fig. 19** The wave spectra obtained by 94th peak wave period corresponding to the runs starting from the same wave spectrum but with a different random set of initial phases. *Thick curve* corresponds to the spectrum averaged over ensemble, *dashed curve* characterizes dispersion of the data

model is still underway. We are also planning to use our model for simulation of more complicated processes.

## 6 Conclusions

In this paper, a straightforward method of the numerical solution of 3D potential wave equations is suggested. The

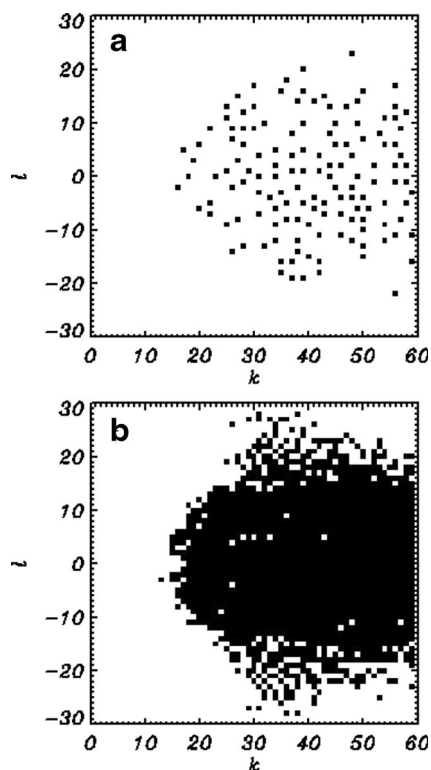


**Fig. 20** *Top panel* shows positions of local maxima in a single spectrum. *Bottom panel* shows position of maxima in 50 parallel runs

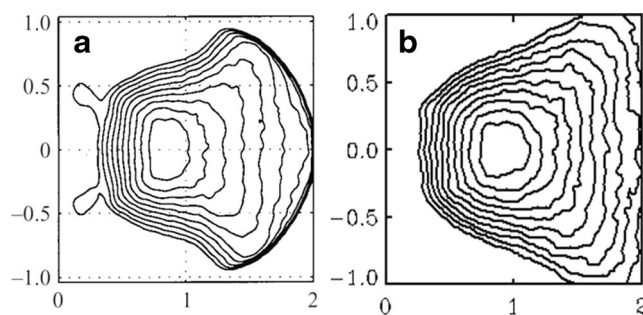


**Fig. 21** The wave spectrum  $\log_{10} S$  in coordinates  $((k/k_p, l/k_p))$ . **a** Calculations of Dysthe et al. (2003) obtained after integration for  $T_p = 95$  wave peak periods and **b** calculation with model (11)–(13) obtained after integration for  $T_p = 67$ . Both spectra are normalized by their maximum value

method uses a surface-following coordinate system. In the new coordinates, the kinematic and dynamic conditions on surface become more complicated, but if we consider them as the evolutionary equations for the surface potential and elevation, we come to the conclusion that these conditions can be easily integrated in the same way as the similar 1D equations in the conformal coordinates. However, calculations of the vertical derivative of the potential on the surface become more complicated, since the Laplace equation for the 3D velocity potential turns into the elliptic equation that should be solved at every time step, which requires a use of extensive computer resources. However, it should be noted that this problem is still much simpler than, for example, standard simulations of the 3D Navier–Stokes equations (or large eddy simulation (LES) equations) in the curvilinear coordinates when a problem of solving the elliptic equation for pressure arises.

The potential wave problem gives a unique opportunity for validation of a full nonlinear model by comparison with the exact stationary solution obtained in a moving coordinate system. This solution is obtained with a completely different algorithm; hence, such validation can be considered as full, nontrivial, and exact. Since the model uses a finite-difference approximation in the vertical direction, we can not expect a perfect agreement between the exact and approximate solutions, though the results of such comparison are quite convincing. A structure of the Stokes wave was supported over a long interval of integration. If the numerical scheme were not accurate enough, an evolution of modes would exhibit a chaotic behavior and the Stokes wave would quickly disintegrate due to the numerical instability. Such evolution was observed many times in the course of development of codes. The scheme is consistent, since with increase of the resolution, its accuracy increases. Note that highly efficient method by Clamond and Grue (2001) has been generalized to 3D finite variable water depth by Fructus and Grue (2007). Currently, we investigate a

possibility of application of the model to the finite depth problem. Such idea is based on presentation of the analytic component of the surface potential in the following form:

$$\bar{\Phi}(\xi, \vartheta, \zeta) = \sum_{k,l} \bar{\varphi}_{k,l} \frac{\cos(|k|(\zeta + H))}{\cos(|k|H)} \Theta_{k,l}, \quad (45)$$

where  $H$  is depth. Because the nonlinear component of velocity potential attenuates with depth faster than the analytical one, a scheme of the solution remains essentially the same.

The model was used here for simulation of the evolution of a steep Stokes wave train with the superimposed initial noise. In case of the directional wave fields, it was shown that an evolution of a wave field occurs in a different way, as compared to that of a unidirectional case, i.e. the new developing modes are oblique toward propagation of a carrier wave.

The most disappointing and unexpected property of the wave model is that the results depend essentially on the initial set of phases; hence, the most reliable results can be obtained with the ensemble modelling. Such simulation can be effectively done in parallel processors. It is not excluded that the stable and smooth results can be obtained by introducing the local viscosity in the Fourier space. Currently, it is unclear in what way this property can be brought into correlation with the natural process. However, we came to conclusion that the primary physical variables are rather the fields of velocity (in the potential assumption, it is a velocity potential) and elevation. The Fourier modes are the result of a formal presentation of wave fields, while they not necessarily present the real objects.

The numerical experiments are performed under quasi-adiabatic conditions. However, the model is designed for investigation of the nonlinear mechanics of the 2D surface waves, particularly for investigation of the extreme waves. After implementation of the energy input scheme and wave breaking parameterization, the model can be used for direct simulations of a 2D wave field evolution under the action of wind, nonlinear interactions, and dissipation. This model can be combined with the 3D LES model for the atmospheric wave boundary layer, being formulated in the same coordinate system. Such approach can be considered as an ultimate solution of the wind–wave interaction problem.

All of the numerical results presented in the current work were obtained using a standard one-processor Dell computer with a speed of 3.00 GHz. Since the model is based in the Fourier transform method, a parallel version of the model does not provide many advantages, while parallel processors are convenient to simultaneously run many versions of the same model, as well as to perform the ensemble modeling.

**Acknowledgments** The authors thank Dr. S. Suslov who made useful comments and Mrs. O. Chalikova for her assistance in preparation of the manuscript. The work was supported by RFBR, grant no. 11-05-0052 and Australian Research Council, Discovery grants DP1093349 and DP130100227.

## References

- Asaithambi NS (1987) Computation of free-surface flows. *J Comp Phys* 73:380–394
- Babanin AV, Babanina AV, Chalikov D (2014) Interaction of surface waves at very close wavenumbers. *Ocean Dyn*. doi:10.1007/s10236-014-0727-4
- Benjamin TB, Feir JE (1967) The disintegration of wave trains in deep water. *J Fluid Mech* 27:417–430
- Bingham HB, Zhang H (2007) On the accuracy of finite-difference solutions for nonlinear water waves. *J Eng Math* 58:211–228
- Cai X, Petter H, Langtangen HP, Nielse BF, Tveito AA (1998) Finite element method for fully nonlinear water waves. *J Comp Phys* 143: 544–568
- Chalikov D (2005) Statistical properties of nonlinear one-dimensional wave fields. *Nonlinear Process Geophys* 12:1–19
- Chalikov D (2007) Numerical simulation of Benjamin-Feir instability and its consequences. *Phys Fluid* 19:016602
- Chalikov D (2009) Freak waves: their occurrence and probability. *Phys Fluid* 21:076602. doi:10.1063/1.3175713
- Chalikov D, Rainchik S (2011) Coupled numerical modelling of wind and waves and the theory of the wave boundary layer. *Boundary-Layer Meteorol* 138:1–41. doi:10.1007/s10546-010-9543-7
- Chalikov D, Sheinin (1998) Direct modeling of one-dimensional nonlinear potential waves. *Nonlinear Ocean Waves*, ed. W. Perrie, *Advances in Fluid Mechanics* 17:207–258
- Chalikov D, Sheinin D (2005) Modeling of extreme waves based on equations of potential flow with a free surface. *J Comp Phys* 210: 247–273
- Clamond D, Grue J (2001) A fast method for fully nonlinear water wave dynamics. *J Fluid Mech* 447:337–355
- Clamond D, Fructus D, Grue J, Kristiansen O (2005) An efficient method for three-dimensional surface wave simulations. Part II: generation and absorption. *J Comp Phys* 205:686–705
- Clamond D, Francius M, Grue J, Kharif C (2006) Long time interaction of envelope solitons and freak wave formations. *Eur J Mech B/ Fluids* 25:536–553
- Dommermuth D, Yue D (1987) A high-order spectral method for the study of nonlinear gravity waves. *J Fluid Mech* 184:267–288
- Dysthe KB (1979) Note on a modification to the nonlinear Schrödinger equation for application to deep water waves. *Proc R Soc Lond A* 369:105–114
- Dysthe KB, Krogstad HE, Soquet-Juglard H (2003) Evolution of a narrow-band spectrum of random surface gravity waves. *J Fluid Mech* 478:1–10
- Engsig-Karup AP, Bingham HB, Lindberg O (2009) An efficient flexible-order model for 3D nonlinear water waves. *J Comp Phys* 228:2100–2118
- Fochesato C, Dias F, Grill S (2006) Wave energy focusing in a three-dimensional numerical wave tank. *Proc R Soc A* 462:2715–2735
- Fructus D, Grue J (2007) An explicit method for the nonlinear interaction between water waves and variable and moving bottom topography by Fructus and Grue. *J Comp Phys* 207(222):720–739
- Fructus D, Clamond D, Grue J, Kristiansen Ø (2005) An efficient model for three-dimensional surface wave simulations. Part I: free space problems. *J Comp Phys* 205:665–685



- Grilli S, Guyenne P, Dias F (2001) A fully nonlinear model for three-dimensional overturning waves over arbitrary bottom, *Int. J. Num Methods Fluids* 35:829–867
- Hausling HJ, Van Eseltine RT (1975) Finite-difference methods for transient potential flows with free surfaces, in: *Proceedings of the International Conference on Numerical Ship Hydrodynamics*, Univ. Extension Publ., Berkely, pp. 295–313
- Lake BM, Yuen HC (1978) A new model for nonlinear wind waves. Part 1. Physical model and experimental results. *J Fluid Mech* 88:33–62
- McLean JW (1982) Instability of finite amplitude water waves. *J Fluid Mech* 14:315–330
- Pierson WJ, Moscowitz L (1964) A proposed spectral form for fully developed wind seas based on the similarity theory of S A Kitaigorodskii. *J Geophys Res* 69(24):5181–5190
- Sheinin D, Chalikov D (2000) Hydrodynamical modeling of potential surface waves. In: *Problems of hydrometeorology and environment on the eve of XXI century. Proceedings of international theoretical conference*, St. Petersburg, June 24–25, 2000, St.-Petersburg
- Stokes GG (1847) On the theory of oscillatory waves. *Trans Cambridge Philos Soc* 8:441–445, *Math. Phys. Pap.*, 1847, 1, 197 – 229
- Su MY (1982) Three-dimensional deep-water waves. Part 1. Experimental measurement of skew and symmetric wave patterns. *J Fluid Mech* 124:73–108
- Thomas LH (1949) Elliptic problems in linear differential equations over a network. *Watson Sci. Comput. Lab Report*, Columbia University, New York
- West B, Brueckner K, Janda R, Milder M, Milton R (1987) A new numerical method for surface hydrodynamics. *J Geophys Res* 92: 11 803–11 824
- Yeung RW (1982) Numerical methods in free-surface flows, *Annual Review of Fluid Mechanics*, 14, Annual Reviews, Palo Alto, CA, 395–442
- Zakharov VE (1968) Stability of periodic waves of finite amplitude on the surface of deep fluid. *J Appl Mech Tech Phys JETP (English translation)* 2:190–194
- Zakharov VE, Dyachenko AI, Vasilyev OA (2002) New method for numerical simulation of a nonstationary potential flow of incompressible fluid with a free surface. *Eur J Mech B/Fluids* 2002(21): 283–291